Squint Spotlight SAR Imaging by Two-Step Scaling Transform-Based Extended PFA and 2-D Autofocus

Shengliang Han [ID], Daiyin Zhu [ID], *Member, IEEE*, and Xinhua Mao [ID], *Member, IEEE*

Abstract—In this article, a novel imaging algorithm by combining two-step scaling transform (TSST) with structure-aided 2-D autofocus is proposed for the squint spotlight synthetic aperture radar (SAR). First, on the basis of planar wavefront assumption, a modified range-frequency linear scaling transform (MRFLST) and an azimuth-time nonlinear scaling transform (ATNST) are proposed to eliminate the coupling between range-frequency and azimuth-time of the received echo. Furthermore, to improve the efficiency, the MRFLST is implemented by using the principle of chirp scaling (PCS), which involves only complex multiplications and fast Fourier transforms (FFTs) without any interpolation, meanwhile, a constant scaling factor (CSF) selecting criteria is defined to avoid range spectrum aliasing. Then, to correct the phase error caused by the range measurement error and atmospheric propagation effects, the prior 2-D phase error structure implied in the TSST is analyzed. Finally, by integrating the derived 2-D phase error structure and range frequency fragmentation technique, a new 2-D autofocus algorithm is presented to improve the image quality. Simulated and real data experiments are carried out to verify the proposed algorithm.

Index Terms—2-D autofocus, planar wavefront assumption, principle of chirp scaling (PCS), range frequency fragmentation, two-step scaling transform.

I. INTRODUCTION

BENEFITING from the unique all-weather and all-time detecting ability, synthetic aperture radar (SAR) becomes the popular and extensively adopted means in supervising and imaging interesting areas [1]. The spotlight mode SAR can provide us with high resolution through continuously adjusting the antenna beam of the radar pointing to a preselected district in time of the echo acquisition [2].

The coherence of data processing over the whole aperture synthesis period is the assurance for getting a well-focused imaging result and the imaging processes require precise measuring positions of the radar footprints. However, the ubiquitous

motion measurement error and atmospheric propagation effects bring disturbances to the signal processing [3], [4]. The induced phase error introduces two kinds of degradations to the formed SAR image, e.g., azimuth phase error (APE) and residual range cell migration (RCM) [5]. Commonly, the residual RCM is assumed to be neglected for the reason that it usually would not exceed one range resolution cell under the small measuring error or intermediate resolutions, in these cases, only APE should be considered. Nevertheless, as the resolution improves or the measurement error increases, the aforementioned assumption is no longer satisfied, the residual RCM and APE should be both taken into consideration.

To solve this problem, the data-driven autofocus, which exploits the phase history data to estimate and remove the phase error, are considered by many to be the workhorse. Among these algorithms, two types of 2-D autofocus methods are enabled to remove both the APE and the RCM, e.g., blind, structure-aided autofocus. The blind approaches calculate the 2-D phase error in a blind way under no presumptions to the relation between residual RCM and APE [6], [7], [8], [9], [10]. Two drawbacks limit the applications of the blind approaches. First, the available redundancy in estimating the 2-D phase error is much less than 1-D phase error estimation. Second, the computational complexity increases with the incremental dimensions of the estimated parameters. The structure-aided approaches [11], [12], [13], [14], [15], also referred to as semiblind autofocus, estimate the 2-D phase error by exploiting the underlying mapping relation between APE and residual RCM, where the 2-D phase error estimation is simplified to the 1-D estimation problem of APE. It is worth noting that, for the structure-aided 2-D autofocus, different imaging algorithms have different 2-D phase error structures.

Because of the 2-D phase error structure is directly determined by the adoptive imaging algorithm, the selection of the imaging algorithm plays a decisive role in the structure-aided 2-D autofocus. In squint SAR imaging, the severe range-azimuth coupling characteristic makes the image focusing much more complicated and challenging than the broadside mode, voiding the classical image formation algorithms, such as range-Doppler algorithm (RDA) [16] and chirp scaling algorithm (CSA) [17]. While many improved versions have been presented for the squinted mode, the increased higher order terms needed to be considered make these algorithms more complicated [18]. The back-projection (BP) algorithm and its modifications [19], [20], [21], [22] are regarded as effective for arbitrary trajectories. Nevertheless, the resulting huge amounts of calculations restrict their practical

applications. In view of the excellent performance of low computational complexity and simple processing chains, the polar format algorithm (PFA) is extensively applied in current airborne SAR missions [23], [24], [25]. It is regarded as the balanced method by many, and it can achieve accurate range cell migration correction (RCMC) in processing ultrahigh resolution SAR data by approximating the spherical wavefront of transmitted signal with the planar wavefront [26].

In this article, to have the same capacities of low computational complexity and simple processing steps as the PFA, the approximation of planar wavefront is also considered to be the premise of the proposed algorithm. Next, a novel two-step scaling transform (TSST), including a modified range-frequency linear scaling transform (MRFLST) with a subsequent azimuth-time nonlinear scaling transform (ATNST), is presented to eliminate the variate coupling between azimuth time and range frequency. To avoid range interpolation, the traditional range-frequency scaling transform (TRFST) can be performed without interpolation by using the principle of chirp scaling (PCS) [27], [28]. Nevertheless, the PCS-based TRFST causes range spectrum aliasing when the azimuth and elevation angles are large. In this article, through multiplying the range frequency by a constant scaling factor (CSF), the PCS-based MRFLST is presented to avoid range interpolation and range spectrum aliasing. Meanwhile, the selection criterion of the required minimum value of CSF is also defined. Then, the ATNST is derived to eliminate the residual coupling between the azimuth-time and the range-frequency. Finally, the fast Fourier transforms (FFTs) can be used to form the final focused image. The proposed imaging algorithm can achieve the same low computational complexity and simple processing chains as the PFA.

Next, to alleviate the 2-D defocus, the prior 2-D phase error structure implied in the TSST is analyzed. The derived 2-D error structure allows us to only calculate the azimuth phase error, then, the 2-D phase error can be acquired straightly through the structure relation. Accordingly, the estimated precision of APE determines the performance of the proposed 2-D autofocus algorithm. Further, in order to reduce the impact of the residual RCM to the estimation of the APE, a range frequency fragmentation technique similar to the spatial frequency domain fragmentation [15] is proposed to estimate the APE in conjunction with phase gradient autofocus (PGA). Cause of different range frequency fragments distribute in different range frequency bands, the estimated APE of different fragments cannot be regarded as the standard APE. To solve this problem, the mapping relations are derived to scale the extracted APEs to the standard APEs, and then the generated standard APEs are averaged to obtain the final estimated APE. Finally, by integrating the derived 2-D phase error structure and the range frequency fragmentation technique, a new 2-D autofocus algorithm is presented to acquire and compensate the 2-D defocus.

The rest of this article is organized as follows. The planar wavefront assumption is explained in Section II. In Section III, the TSST is introduced and the PCS-based MRFLST is proposed. In Section IV, a novel 2-D autofocus technique is proposed by taking advantage of the priori structure on the residual 2-D phase error after the TSST. Experimental results
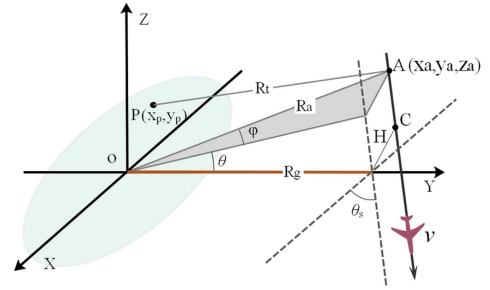

Fig. 1. Data acquisition geometry of the squint spotlight SAR.

are presented in Section V to verify the effectiveness of the proposed algorithm. Section VI discusses the issues of defocus compensation and geometric distortion correction for the proposed TSST. Section VII provides the conclusion in the end.

II. SIGNAL MODEL AND APPROXIMATION

In this section, the SAR geometrical configuration is established and the echo model is discussed and approximated under the planar wavefront assumption, which is the same with the polar format algorithm (PFA).

The SAR data collecting geometry for the squint spotlight mode is shown in Fig. 1. In spotlight mode, the radar steers the beam to still illuminate the fixed area. v represents the radar velocity, t is the slow time, the height of the carrying platform is H. The trajectory center is denoted as C. The projection of the working distance R_0 (OC) onto $X - O - Y$ is represented by R_g. The squint angle is specified as θ_s. An arbitrary point target in the illuminated scene is represented by $P(x_p, y_p, 0)$. The instantaneous elevation and azimuth angle are indicated by the symbols φ and θ, respectively. Meanwhile, the instantaneous positions of radar can be expressed as $x_a = vt \cos \theta_s$, $y_a = R_g + vt \sin \theta_s$, $z_a = H$. Thus, the instantaneous range between the scene center O and the radar can be written as $R_a = \sqrt{x_a{}^2 + y_a{}^2 + z_a{}^2}$ while the instantaneous range between the radar and the point P can be written as $R_t = \sqrt{(x_a - x_p)^2 + (y_a - y_p)^2 + z_a{}^2}$.

Suppose the transmitted signal with a linear frequency modulation, the received echo from target P can be written as

$$S(t, \tau) = w_a \left(\frac{t}{T_a} \right) \cdot w_r \left(\tau - \frac{2R_t}{c} \right)$$

$$\cdot \exp \left[j\pi\gamma \left(\tau - \frac{2R_t}{c} \right)^2 \right] \cdot \exp \left[-j\frac{4\pi f_c}{c} R_t \right] \tag{1}$$

where w_a and w_r represent the azimuth and range envelope, τ is the fast time, T_a denotes the synthetic aperture time, f_c denotes the carrier frequency, γ represent the chirp rate, c is the light speed.

Apply FFT to τ and then perform the identical procedures of matched filtering and azimuth dechirp in PFA [29] by multiplying the phase terms $\exp(j\pi\frac{f_r^2}{\gamma}) \cdot \exp[j\frac{4\pi}{c}(f_c + f_r)R_a]$, the

received echo (ignore the envelopes) can be expressed as

$$S(t, f_r) = \exp\left[j\frac{4\pi}{c}(f_c + f_r)\Delta R\right] \quad (2)$$

where $\Delta R = R_a - R_t$ is the differential range. Using the planar wavefront assumption [14], ΔR can be simplified to

$$\Delta R \approx \Delta R_p = \cos\varphi\sin\theta \cdot x_p + \cos\varphi\cos\theta \cdot y_p \quad (3)$$

where $\cos\varphi\sin\theta = x_a/R_a$, $\cos\varphi\cos\theta = y_a/R_a$. Substituting ΔR with ΔR_p, the signal in (2) is updated as

$$S_p = \exp\left[jk_r\left(\cos\varphi\sin\theta \cdot x_p + \cos\varphi\cos\theta \cdot y_p\right)\right] \quad (4)$$

where $k_r = \frac{4\pi}{c}(f_c + f_r)$ represents the wavenumber, the range and azimuth spatial frequency can be respectively defined as $k_y = k_r\cos\varphi\cos\theta$ and $k_x = k_r\cos\varphi\sin\theta$. Because of θ and φ are functions of azimuth time, it is apparent that the coupling between azimuth time and range frequency in (4) can be divided into two parts, i.e., the x_p related coupling and the y_p related coupling. Accordingly, to focus the target, the y_p and x_p related coupling should be both eliminated.

III. IMAGING WITH TWO STEP SCALING TRANSFORM

In this section, to eliminate the coupling between azimuth-time and range-frequency, the TSST, including MRFLST with a subsequent ATNST, is presented in this section. Furthermore, to improve the efficiency, the MRFLST is implemented by the PCS, which involves only complex multiplications and FFTs without any interpolation, meanwhile, the CSF selection criteria of the MRFLST is also defined to avoid range spectrum aliasing.

A. Traditional Range-Frequency Scaling Transform

From (4), the y_p related coupling phase is extracted as

$$\Psi_y(t, f_r) = k_r \cdot \cos\varphi\cos\theta$$

$$= k_r \cdot \frac{R_g + vt\sin\theta_s}{\sqrt{(vt\cos\theta_s)^2 + (R_g + vt\sin\theta_s)^2 + H^2}} \quad (5)$$

A slow-time Taylor series expansion on (5) is performed such that

$$\Psi_y(t, f_r) = k_r \cdot \left[\cos\varphi_0 + C_y^L(t) + C_y^R(t)\right] \quad (6)$$

where

$$\begin{cases} C_y^L(t) = \frac{v\sin\theta_s\sin\varphi_0{}^2}{R_0} \cdot t \\ C_y^R(t) = \cos\varphi\cos\theta - \cos\varphi_0 - C_y^L(t) \end{cases}$$

where $C_y^L(t)$ and $C_y^R(t)$ can be regarded as the linear and the residual high-order coupling, respectively.

According to [27], the range resampling of the PFA is essentially a range frequency scaling transform, that is to say, the y_p related coupling can be eliminated by TRFST

$$f_r = \delta_r\hat{f}_r + f_c(\delta_r - 1) \quad (7)$$

where $\hat{f}_r$ denotes the scaled range frequency variable, and the scaling factor δ_r is defined as

$$\delta_r = \frac{\cos\varphi_0}{\cos\varphi\cos\theta} \quad (8)$$

where φ_0 is the elevation angle at the center radar footprint.

Inserting (7) into (4), the echo can be expressed as

$$S_p(t, \hat{f}_r) = \exp\left[j\frac{4\pi}{c}(f_c + \hat{f}_r)\right.$$
$$\left. \cdot (\cos\varphi_0\tan\theta \cdot x_p + \cos\varphi_0 \cdot y_p)\right] \quad (9)$$

where

$$\tan\theta = \frac{x_a}{y_a} = \frac{vt\cos\theta_s}{R_g + vt\sin\theta_s}.$$

It can be obviously seen that the y_p related azimuth-time and range-frequency is decoupled completely.

B. Modified Range-Frequency Linear Scaling Transform

To avoid range interpolation, the TRFST can be realized by using the PCS [27], [28]. Nevertheless, the PCS-based TRFST will cause range spectrum aliasing when δ_r is large. To address this problem, we propose a constant scaling factor (CSF) aided modified range-frequency linear scaling transform (MRFLST) in this section.

The CSF-$\boldsymbol{\beta}$ aided MRFLST is defined as

$$f_r = \delta_r\tilde{f}_r \cdot \boldsymbol{\beta} + f_c(\delta_r - 1) \quad (10)$$

where $\tilde{f}_r$ represents the scaled range frequency variable. $\boldsymbol{\beta}$ is the introduced CSF. Inserting (10) into (4), the echo is transformed to

$$S_{pr}(t, \tilde{f}_r) = \exp\left[j\frac{4\pi}{c}\left(f_c + \boldsymbol{\beta}\tilde{f}_r\right)\right.$$
$$\left. \cdot (\cos\varphi_0\tan\theta \cdot x_p + \cos\varphi_0 \cdot y_p)\right]. \quad (11)$$

It is apparent that the y_p related coupling is also disappeared and the x_p related coupling is altered by the MRFLST.

Meanwhile, the altered x_p related coupling phase can be extracted as

$$\Psi_x(t, \tilde{f}_r) = \tilde{k}_r \cdot \cos\varphi_0\tan\theta \quad (12)$$

where, $\tilde{k}_r = \frac{4\pi}{c}(f_c + \boldsymbol{\beta}\tilde{f}_r)$ is the new wavenumber. The same as (5), a temporal Taylor series expansion on (12) is performed such that

$$\Psi_x(t, \tilde{f}_r) = \tilde{k}_r \cdot \cos\varphi_0 \cdot \left[C_x^L(t) + C_x^R(t)\right] \quad (13)$$

where

$$\begin{cases} C_x^L(t) = \frac{v\cos\theta_s}{R_g} \cdot t \\ C_x^R(t) = \tan\theta - C_x^L(t) \end{cases}$$

where $C_x^L(t)$ and $C_x^R(t)$ denote the linear and residual high-order RCM, respectively.

To intuitively indicates the aforementioned analysis, the variations of $C_y^L(t)$ and $C_y^R(t)$ of Ψ_y before and after MRFLST for
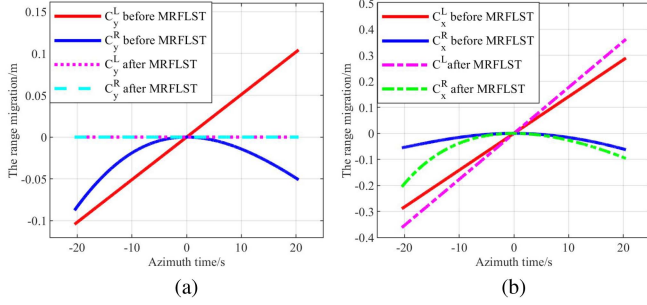
Fig. 2. Linear and residual high-order terms of coupling before and after MRFLST. (a) y_p related coupling. (b) x_p related coupling.

TABLE I
SIMULATION PARAMETERS

Parameters	Values
Carrier frequency	400 MHz
Pulse duration	2 μs
Wavelength	0.75 m
PRF	100 Hz
Range band width	300 MHz
Squint angle θ_s	45°
Operating distance	5 km
Radar velocity	140 m/s

a squint SAR system are illustrated in Fig. 2(a). Table I displays the relevant simulation parameters. The short working distance and long wavelength are unlikely to happen synchronously in practical application, but they are adopted here to illustrate the variation of the RCM trajectory during the various stages of the TSST. The variation of $C_x^L(t)$ and $C_x^R(t)$ before and after MRFLST for the squint SAR system parameters in Table I are shown in Fig. 2(b).

Compared (9) with (11), it is apparent that both TRFST and MRFLST can correct the y_p related coupling and change the x_p related coupling. The only difference between (9) and (11) is the CSF-$\boldsymbol{\beta}$. After TRFST, the range spatial frequency in (9) can be denoted as $\hat{k}_y = \frac{4\pi}{c}(f_c + \hat{f}_r)\cos\varphi_0$, where the output interval cannot be changed. Nevertheless, when the range dimensional processing is implemented by interpolation, the spatial frequency interval of the PFA can be altered for different range resolution demand [2]. From this perspective, the TRFST can be regarded as an incomplete equivalence relation to the range resampling of the PFA. After MRFLST, the range spatial frequency in (11) can be denoted as $\widetilde{k}_y = \frac{4\pi}{c}(f_c + \boldsymbol{\beta}\hat{f}_r)\cos\varphi_0$, where the output interval can be flexibly selected by altering the value of $\boldsymbol{\beta}$. Consequently, the MRFLST can be regarded as the complete equivalence relation to the range resampling of the PFA.

C. Interpolation-Free Implementation of MRFLST

To avoid range spectrum aliasing caused by the PCS-based TRFST, the PCS-based MRFLST, and the selection criterion of the required minimum value of CSF-$\boldsymbol{\beta}$ are given in this section.
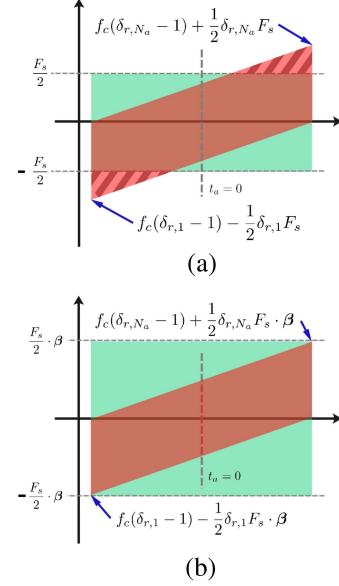

Fig. 3. Variation of range frequency before and after the range frequency scaling transform. (a) TRFLST (or MRFLST, $\boldsymbol{\beta} = 1$). (b) MRFLST, $\boldsymbol{\beta} = \text{Max}[\cdot]$.
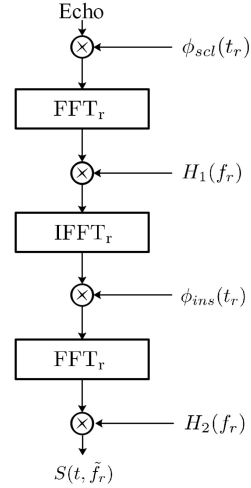

Fig. 4. Implementation of MRFLST by using PCS.

Before introducing the selection criterion of $\boldsymbol{\beta}$, the origin of the spectrum aliasing is first analyzed. The root of range spectrum aliasing is that the range frequency exceeds range sampling rate. This problem is shown in Fig. 3(a), where N_a is the size of total pulses, F_s is the sampling rate of the A/D converter. $\delta_{r,1}$ and δ_{r,N_a} represent the values of δ_r at the moments of the $1th$ and the $N_a th$ pulses.

Recall (8), the numerical value of δ_r is inversely proportional to the product of $\cos\phi$ and $\cos\theta$. When δ_r is growing bigger, the offset of the center frequency $f_c(\delta_r - 1)$ in (7) is getting bigger, which will result in the scaled range frequency exceeding the sampled frequency band (the sampling rate is not satisfy requirement), as seen in the Fig. 3(a). The green area represents the frequency band of observation $[-\frac{1}{2}F_s, \frac{1}{2}F_s]$. The red area represents the frequency after scaling. The nonoverlapping red

areas (two triangles marked by stripes) represent the parts exceeded the observed frequency band, which will lead to spectrum aliasing after chirp scaling operation.

In this article, this problem can be easily solved by selecting proper value of β. To eliminate the spectrum aliasing, the CSF-β should satisfy

$$\beta \geq \mathbf{Max}\left[\beta_1, \beta_2, 1\right] \tag{14}$$

where

$$\beta_1 = \frac{2f_c(\delta_{r,N_a} - 1) + F_s}{\delta_{r,N_a} \cdot F_s}$$

$$\beta_2 = \frac{F_s - 2f_c(\delta_{r,1} - 1)}{\delta_{r,1} \cdot F_s}. $$

For the proposed MRFLST ($\beta = Max[\cdot]$), seen in Fig. 3(b), the observed range frequency scope is extended to $[-\frac{1}{2}F_s \cdot \beta, \frac{1}{2}F_s \cdot \beta]$. The constant factor β improves the sampling frequency in range dimension and further avoids the spectrum aliasing during the chirp scaling operation.

The realization processes of the PCS-based MRFLST are shown in Fig. 4. The inside functions are given as

$$\begin{cases} \phi_{scl}(t_r) = \exp\left[-j\pi\gamma\frac{\beta\delta_r - 1}{\beta\delta_r}\left(t_r - \frac{2R_a}{c}\right)^2\right] \\ H_1(f_r) = \exp\left(j\frac{\pi\beta\delta_r}{\gamma}f_r^2\right) \\ \phi_{ins}(t_r) = \exp\left[j\pi\gamma\frac{\beta\delta_r - 1}{\beta^2\delta_r^2}\left(t_r - \frac{2R_a}{c}\right)^2\right] \\ \qquad\qquad \cdot \exp\left[-j2\pi\frac{f_c(\delta_r - 1)}{\beta\delta_r}t_r\right] \\ H_2(f_r) = \exp\left[j\frac{4\pi}{c}\left(f_r + f_c\frac{\delta_r - 1}{\beta\delta_r}\right)R_a\right] \\ \qquad\qquad \cdot \exp\left(j\frac{4\pi f_c}{c}R_a\right) \end{cases} \tag{15}$$

where the input signal at the start of Fig. 4 is the received echo in (1) and β plays an important role in preventing the spectrum aliasing. It should be noted that the procedures of match filtering and azimuth dechirp before (2) are integrated into the PCS-based MRFLST.

D. Azimuth-Time Nonlinear Scaling Transform

To eliminate the x_p related coupling in (11), we propose an azimuth-time nonlinear scaling transform (ATNST)

$$t = \frac{f_c}{f_c + \beta\tilde{f}_r + \alpha \cdot \zeta \cdot \eta} \cdot \zeta \cdot \eta. \tag{16}$$

The symbol ζ denotes a constant scaling factor, which can be used to change the azimuth resolution of the final image by sacrificing part of the data like PFA [2], and the symbol α is defined as

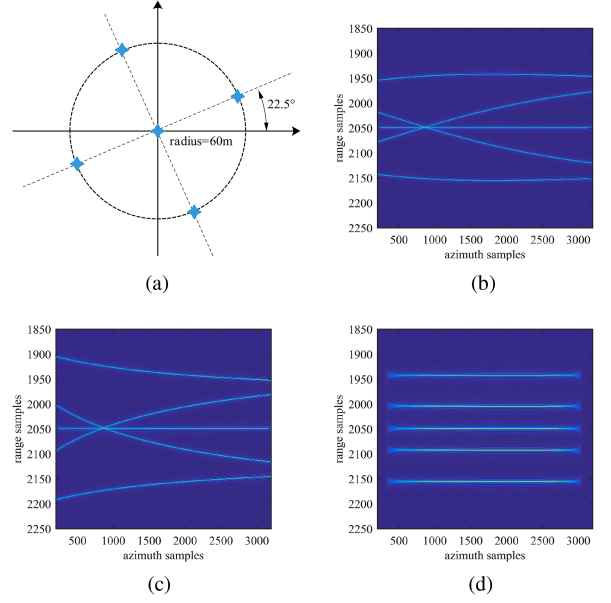$$\alpha = -\frac{v f_c \sin\theta_s}{R_g}. \tag{17}$$

Fig. 5. Range compressed results in different processing stages of the TSST under squint mode. (a) Overall distribution of simulated point targets. (b) Directly range compressed. (c) After MRFLST. (d) After ATNST.

Inserting (16) into (11), the signal can be written as

$$S_{pra}(\eta, \tilde{f}_r) = \exp\left\{j\left[\frac{4\pi f_c}{c}\frac{\cos\varphi_0 \cos\theta_s v}{R_g} \cdot \zeta \cdot \eta \cdot x_p \right.\right.$$
$$\left.\left. + \frac{4\pi}{c}(f_c + \beta\tilde{f}_r)\cos\varphi_0 \cdot y_p\right]\right\}. \tag{18}$$

It can be concluded from (18) that the x_p related coupling is eliminated by the proposed ATNST. Based on the parameters in Table I, the range compressed results in different processing procedures of the proposed TSST are shown in Fig. 5. After the TSST, the FFT can be utilized to generate the final focused SAR image.

E. Algorithm Summary and Complexity Analysis

Fig. 6 gives the main flow diagrams of the proposed TSST and the PFA. It can be seen that both the TSST and the PFA have two major steps, i.e., the range resampling and the azimuth resampling. The essences of the two algorithms are the same. The distinction between the two algorithms is that the PFA resample the spatial frequency domain data from polar to rectangular grid $(k_x \to \tilde{k}_x, k_y \to \tilde{k}_y)$ from the perspective of the use of FFTs, but the presented TSST resample the data by scaling azimuth-time and range-frequency from the viewpoint of rang-azimuth variate decoupling.

The azimuth resampling of the PFA is to resample the azimuth spatial frequencies from the nonuniform spacing to uniform spacing, which is essentially a nonuniform-to-uniform resampling. The azimuth resampling (ATNST) of the proposed method
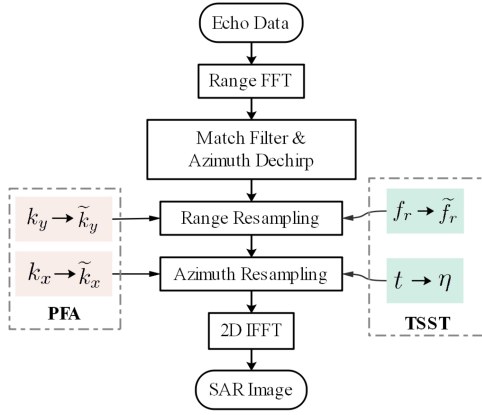
Fig. 6.   Flow diagrams of the PFA and the presented TSST.

is to resample the azimuth time from uniform spacing to nonuniform spacing, which is essentially a uniform-to-nonuniform resampling.

Supposing a real multiplication or a real addition as one operation, the cost of a length-N FFT requires $5Nlog_2 N$ operations. *8-point sinc* function is selected as the interpolation kernel (three real additions and four multiplications for a point). To obtain an $N \times N$ pixel imagery from received echo containing N fast time and N slow (azimuth) time samples: for the classical PFA, the range FFT, range interpolation, azimuth interpolation and 2-D IFFT constitute the main part of the computation cost, accordingly, the approximated computational cost of the classic PFA can be defined as $O(15 N^2 log_2 N + 112 N^2)$. Cause of the MRFLST and ATNST can also be easily implemented by interpolation, the estimated computational cost of the proposed TSST can also be defined as $O(15 N^2 log_2 N + 112 N^2)$. Consequently, on the basis of interpolation implementation, the proposed method is able to reach the same computational efficiency as the classical PFA.

Additionally, the range resampling $f_r \to \tilde{f}_r$ in the proposed algorithm can be implemented by PCS (the procedure is shown in Fig. 4), which mainly contains three times FFTs and the required computational cost can be calculated as $O(15 N^2 \log_2 N)$. In this case, the computational cost of the proposed range PCS-based TSST can be estimated as $O(25 N^2 log_2 N + 56 N^2)$. Further, cause of no interpolation used in the range dimensional processing, it is suitable for practical applications by dedicated devices, such as DSP and FPGA, to realize real-time imaging.

IV. STRUCTURE-AIDED 2-D AUTOFOCUS

In the aforementioned derivations of the TSST, the measured radar coordinates are supposed to be accurately obtained. Nevertheless, in practical SAR systems, especially for airborne SAR, the motion measurement equipment, e.g., global position system (GPS)/inertial measurement unit (IMU), sometimes cannot offer positions with satisfied accuracy. The uncertain motion measurement error, if not compensated, will severely degrade the image quality.

Normally, the phase error generated by motion measurement error will not exceed the range cell, and the azimuth phase error (APE) is the main consideration of the image quality and the 1-D autofocus algorithms are capable of estimating and correcting the APE. Nevertheless, this conclusion becomes invalid as the resolution improves or the measurement error increases, the satisfactory estimation will be unavailable for the 1-D autofocus algorithms. Under such cases, 2-D autofocus technique is regarded as an effective tool to generate well focused SAR images. In this part, we present a comprehensive investigation of the mapping relationship between 2-D phase error and APE by exploiting the TSST, and a novel 2-D autofocus algorithm is presented by combing the 2-D phase error structure and range frequency fragmentation technique.

A. Analytical Derivations to the 2-D Phase Error Structure of TSST

Take the actual situation into account, the received echo with motion measuring error can be modeled as

$$S_e(t, f_r) = \exp\left\{ j\frac{4\pi}{c}(f_c + f_r)\left[R_\Delta + \xi(t)\right] \right\} \qquad (19)$$

where $\xi(t)$ denotes the measuring error. After applying the MRFLST (10), the echo in (19) is rewritten as

$$S_{er}(t, \tilde{f}_r) = \exp\left\{ j\frac{4\pi}{c}(f_c + \boldsymbol{\beta}\tilde{f}_r)\cos\varphi_0 \right.$$
$$\left. \cdot \left[\tan\theta \cdot x_p + y_p + \ell(t)\right] \right\} \qquad (20)$$

where $\ell(t) = \xi(t)/(\cos\varphi \cos\theta)$. After applying the ATNST (16), the signal in (20) turns to

$$S_{era}(\eta, \tilde{f}_r) = S_{pra}(\eta, \tilde{f}_r) \cdot S_{2dp}(\eta, \tilde{f}_r) \qquad (21)$$

where S_{pra} denotes the signal (18) and the 2-D phase error S_{2dp} can be expressed as

$$S_{2dp}(\eta, \tilde{f}_r) = \exp\left[j\frac{4\pi \cos\varphi_0}{c}(f_c + \boldsymbol{\beta}\tilde{f}_r) \right.$$
$$\left. \cdot \ell\left(\frac{f_c}{f_c + \boldsymbol{\beta}\tilde{f}_r + \alpha \cdot \boldsymbol{\zeta} \cdot \eta} \cdot \boldsymbol{\zeta} \cdot \eta \right) \right]. \qquad (22)$$

At this point, the phase of S_{2dp} can be extracted as

$$\Phi(\eta, \tilde{f}_r) = \frac{4\pi\left(f_c + \boldsymbol{\beta}\tilde{f}_r\right)\cos\varphi_0}{c}$$
$$\cdot \ell\left(\frac{f_c}{f_c + \boldsymbol{\beta}\tilde{f}_r + \alpha \cdot \boldsymbol{\zeta} \cdot \eta} \cdot \boldsymbol{\zeta} \cdot \eta \right). \qquad (23)$$

Make $\tilde{f}_r = 0$, the standard azimuth phase error (SAPE) can be defined as

$$\Phi_{ape}^S(\eta) = \frac{4\pi f_c \cos\varphi_0}{c} \cdot \ell\left(\frac{f_c}{f_c + \alpha \cdot \boldsymbol{\zeta} \cdot \eta} \cdot \boldsymbol{\zeta} \cdot \eta \right). \qquad (24)$$

It is well-known that that the SAPE can be easily obtained by using 1-D autofocus. Consulting (23) and (24), the mapping
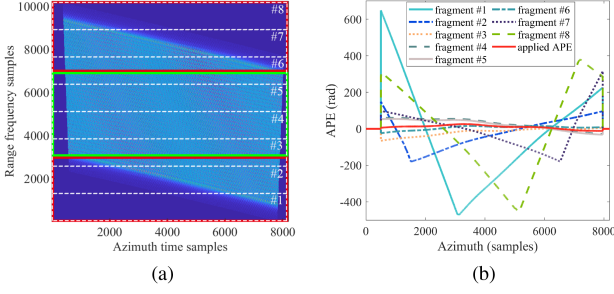
Fig. 7. Spectrum envelope after the proposed two-step scaling transform and APE comparisons of different range fragments. (a) Spectrum shape of highly squinted spotlight SAR after the proposed TSST. (b) Comparisons of the applied and the estimated APEs for different fragments.

relation between the 2-D phase error and the SAPE can be derived as

$$\Phi(\eta, \tilde{f}_r) = \frac{f_c + \boldsymbol{\beta}\tilde{f}_r}{f_c} \Phi_{ape}^S \left(\frac{f_c}{f_c + \boldsymbol{\beta}\tilde{f}_r} \cdot \eta \right). \quad (25)$$

Combing the analytical relationship shown in (24) and (25), to obtain the 2-D phase error, we merely need to obtain the SAPE from the defocused SAR imagery and then mapping it into 2-D structure by applying a keystone-like transform to the SAPE and multiplying a ratio $f_c + \boldsymbol{\beta}\tilde{f}_r/f_c$.

B. SAPE Estimation via Range Frequency Fragmentation

After the above analysis, it can be concluded that the estimate accuracy of the 2-D phase error is fully decided by the SAPE. From (24), SAPE is defined as the 2-D phase error (23) calculated at the range frequency $\tilde{f}_r = 0$. Nevertheless, when the resolution becomes finer or the measured radar positions with very poor precision, the generated RCM will exceed the range cell, which will severely affect the estimation accuracy of SAPE. To improve the estimation accuracy of the SAPE, a direct method is to utilize a small portion of the range history data to produce a low-range resolution image, next, the SAPE is estimated by applying a classical 1-D autofocus method to this partial data [14], [30]. While this processing scheme can realize better performance on error estimation accuracy than the direct 1-D phase error estimation, the utilized a tiny fraction of the collected data cannot furthest reveal the phase error information of the available data. The low data utilization ratio causes a degree of performance loss [15].

To solve this problem, the range frequency fragmentation technique similar to the spatial frequency domain fragmentation [15] is proposed to make good use of the collected data. After the TSST, we split the data into multiple range fragments in the range-frequency and azimuth-time domain, as depicted in Fig. 7(a). Then, PGA is used to obtain the APEs of the different range fragments. In general, the data are assumed to be split into M continuous fragments along the range direction and the center range frequency of the ith fragment is defined as $\tilde{f}_{ri}$. According to (23), make $\tilde{f}_r = \tilde{f}_{ri}$, the APE of the ith fragment

can be expressed as

$$\Phi_i(\eta) = \frac{4\pi(f_c + \boldsymbol{\beta}\tilde{f}_{ri})\cos\varphi_0}{c}$$
$$\cdot \ell\left(\frac{f_c}{f_c + \boldsymbol{\beta}\tilde{f}_{ri} + \alpha \cdot \boldsymbol{\zeta} \cdot \eta} \cdot \boldsymbol{\zeta} \cdot \eta \right), \quad i = 1, 2 \cdots, M. \quad (26)$$

Because of different fragments distribute in different range frequency bands, the estimated APEs ($\tilde{f}_r \neq 0$) cannot be regarded as the SAPE. That is to say, the extracted APE estimates from different fragments cannot be directly used to generate the SAPE. Fortunately, the extracted APEs can be scaled to the SAPE by a ratio $(f_c + \boldsymbol{\beta}\tilde{f}_{ri})/f_c$, and then multiply the scaled APE by the reciprocal of the scaling factor as follows:

$$\Phi_i^S(\eta) = \frac{f_c}{f_c + \boldsymbol{\beta}\tilde{f}_{ri}} \Phi_i \left(\frac{f_c + \boldsymbol{\beta}\tilde{f}_{ri}}{f_c} \cdot \eta \right), i = 1, 2 \cdots, M. \quad (27)$$

Then, the final SAPE can be obtained by averaging the extracted APEs as

$$\Phi_{ape}^S(\eta) = \frac{1}{M} \sum_{n=1}^{N} \Phi_i^S(\eta), \quad i = 1, 2 \cdots, M. \quad (28)$$

It is worth noting that, after the proposed TSST, the spectrum of the squinted spotlight SAR with large squint and elevation angle is no longer symmetrically distributed along the azimuth direction, as seen in Fig. 7(a). Since the spectral envelope of the red rectangle marked areas are similar to extremely irregular (triangle) subband spectrums rather than rectangle, which will severely affect the estimate accuracy of the 1-D autofocus. From Fig. 7(b), we can see that the estimated APEs of fragment #1, #2, #7 and #8 severely deviate the applied APE. Therefore, the spectrum, which will induce irregular envelope, should be abandoned before the range frequency fragment.

The whole flow diagram of the presented imaging and autofocus algorithm is described in Fig. 8. It consists of three main stages, i.e., the PCS-based MRFLST, the ATNST and the 2-D autofocus.

V. EXPERIMENTS AND ANALYSES

A. Performance Verification of the TSST

To demonstrate the imaging ability of the presented TSST, the simulated experiments are carried out in this part. Table II lists the adopted parameters in the experiments. The large squint angle $\theta_s = 70°$, large elevation angle $\varphi_0 = 30°$ and integration angle $8°$ are considered.

Fig. 9 gives the resulting spectrums (azimuth-time and range-frequency domain) after different range dimensional processing schemes. For the interpolation-based methods (the first row in Fig 9), Fig. 9(a) suffers from the effects of spectrum loss, while the spectrum in Fig. 9(b) is intact after the MRFLST with $\boldsymbol{\beta} = Max[\cdot]$. For the PCS-based methods (the second row in Fig 9), the phenomenon of spectrum aliasing occurs in Fig. 9(c) for the PCS-based TRFST (the aliased spectrums are marked by two
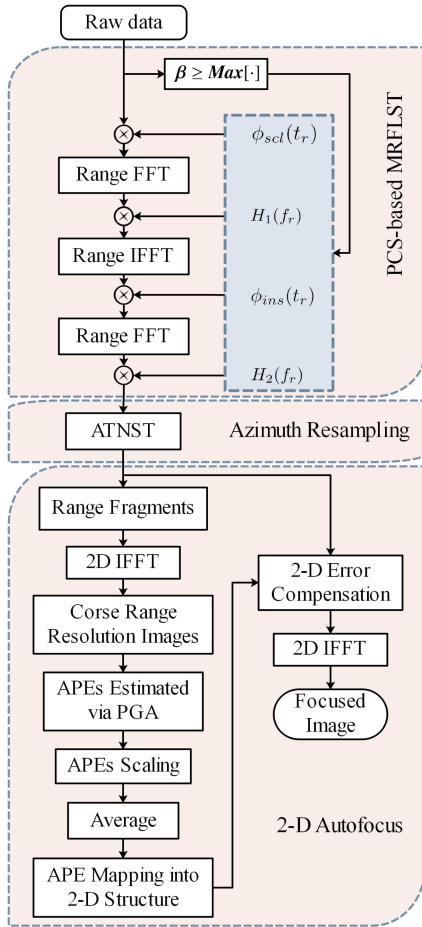
Fig. 8. Whole flow diagram of the presented algorithm.

TABLE II
EXPERIMENT PARAMETERS

Parameter Name	Value
PRF	800 Hz
Radar velocity	180 m/s
Bandwidth	400 MHz
Pulse duration	2 μs
Central squint distance	20000 m
Carrier frequency	10 GHz
Altitude	10000 m
Squint angle	70°

Fig. 9. Resulting spectrums after different range dimensional processing schemes. (a) After interpolation-based TRFST (or MRFLST, when $\beta = 1$). (b) After interpolation-based MRFLST, when $\beta = Max[\cdot]$. (c) After PCS-based TRFST (or MRFLST, when $\beta = 1$). (d) After PCS-based MRFLST, when $\beta = Max[\cdot]$.

Fig. 10. Comparisons of the imaging results. (a) Imaging result of the range PCS-based TRFST (or the range PCS-based MRFLST when $\beta = 1$). (b) Imaging result of the range PCS-based MRFLST when $\beta = Max[\cdot]$.

red triangle), while this problem is well settled by the PCS-based MRFLST with $\beta = Max[\cdot]$ in Fig 9(d).

Fig. 10(a) and (b) shows the final imaging results of Fig. 9(c) and (d), respectively. From Fig. 10(a), we can see that the ghost targets are observed in the final formed image, which is caused by the range spectrum aliasing in Fig. 9(c). Compared Fig. 10(a), it can be found that the ghost targets are not observed in Fig. 10(b). Consequently, it can be concluded that the proposed PCS-based MRFLST can effectively avoid the problem of spectrum aliasing by choosing the proper value of β. To have a better comparison, Fig. 11 provides the 2-D contours of the selected three targets (the red circles marked points A, B, and C in Fig. 10). The left
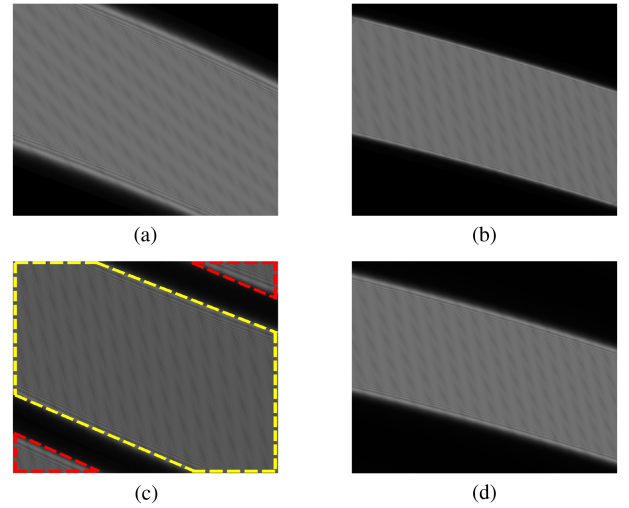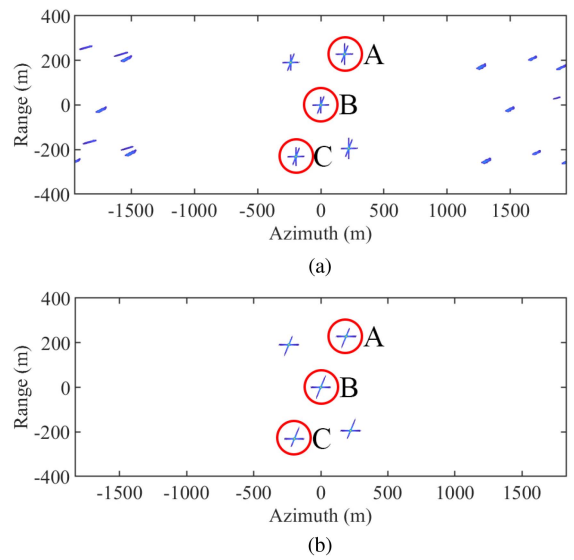
column gives the contour plots of the three targets in Fig. 10(b). The right column shows the contour plots of the three targets in Fig. 10(a). It is evident that the contour plots of Fig. 11(b), (d), and (f) suffer from severe sidelobes degradation, which is also caused by the range spectrum aliasing in Fig. 9(c). The spectral support region of the contour plots is no longer a parallelogram-liked shape [marked by an irregular yellow hexagon in Fig. 9(c)], which results in sidelobes degradation in Fig. 11(b), (d), and (f).

In addition, the spectrum aliasing causes a degree of resolution losses to the imaging results of the PCS-based TRFLST. The azimuth and range profiles of point A for different algorithms are
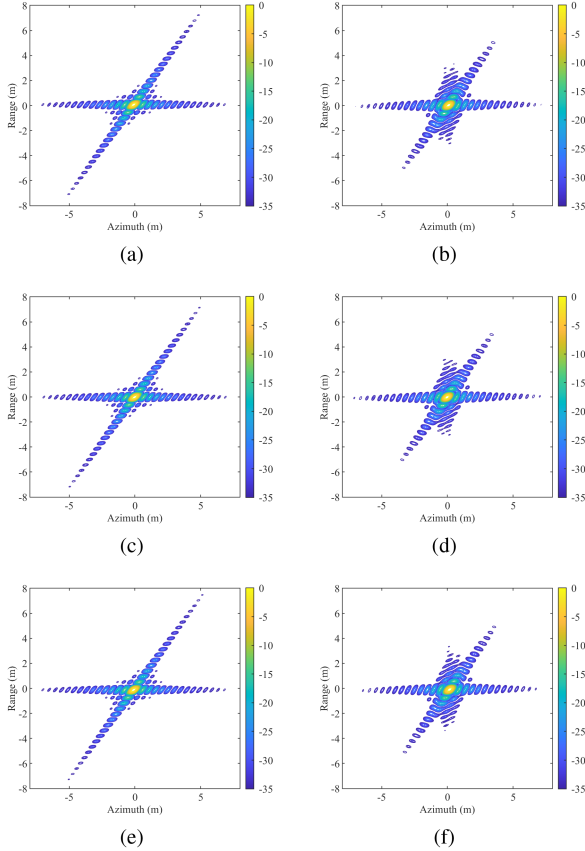
Fig. 11. Contour plots of the selected three targets in Fig. 10. The left column, (a), (c), and (e) gives the contour plots of the selected three point targets A, B, and C after the TSST (PCS-based MRFLST, $\beta = \mathrm{Max}[\cdot]$). The right column, (b), (d), and (f) gives the contour plots of the selected three point targets A, B and C after the TSST (PCS-based TRFST).
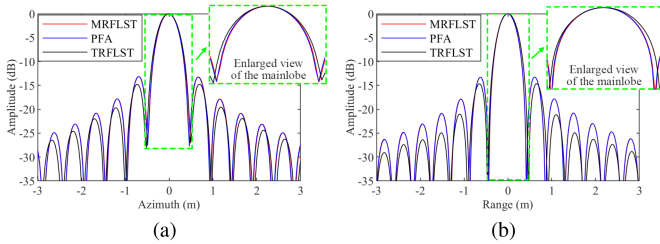

Fig. 12. Comparisons of the azimuth and range profiles of point A. (a) Azimuth profiles of different algorithms. (b) Range profiles of different algorithms.

shown in Fig. 12. It is apparent that the proposed algorithm and the PFA have almost exactly the same focusing quality. Although the PCS-based TRFST (TSST, $\beta = 1$) has a lower side lobe, the main lobe suffers from significant broadening.

B. Performance Verification of the Proposed 2-D Autofocus

1) Simulation Experiment: To demonstrate the derived 2-D phase error structure of the presented TSST, the simulations are carried out in this part. Table III gives the related simulated parameters. In the experiment, three points (i.e., points A, B, and C) are located at different positions. Point A is located at

TABLE III
EXPERIMENT PARAMETERS

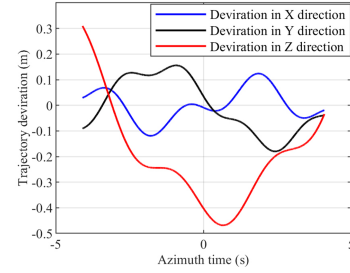| Parameters name	Value
PRF	1000 Hz
Radar velocity	180 m/s
Bandwidth	500 MHz
Pulse duration	2 μs
Central squint distance	20000 m
Carrier frequency	10 GHz
Altitude	10000 m
Squint angle	$60°$

Fig. 13. Flight trajectory deviations in three directions.
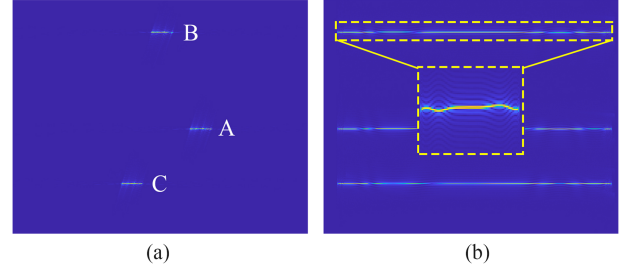

Fig. 14. Imaging results by the TSST when $\beta = \mathrm{Max}[\cdot]$. (a) Final image. (b) Range compressed image.

the center of the illuminated scene. Points B and C are 300 m away from point A. The nominal flight path of the radar, which is used in the imaging process, is assumed to be a straight line. But the deviations in three directions are considered in the process of echo generation, as shown in Fig. 13.

Fig. 14 exhibits the final imaging result and the range-compressed result processed by the TSST directly. It shows that the generated results of the simulated targets are severely affected by 2-D defocus due to the measuring range error. The outline of the three targets cannot be recognized from the smeared imaging results in Fig. 14. To enhance the focusing quality, the PGA is utilized to improve the image quality. The corresponding full compressed result and the range compressed result after PGA are shown in Fig. 15. The image quality is enhanced to some extent, but evident defocus still can be observed in the image. To further improve the image quality, the 2-D phase error is estimated and compensated by applying the proposed 2-D autofocus scheme. The corresponding full compressed result and the range compressed result after the proposed 2-D autofocus are shown in Fig. 16. For comparison, the 2-D contour plots of point A are also exhibit in Figs. 15(a)
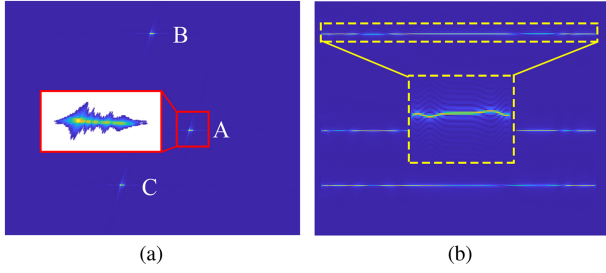
Fig. 15. Refocused results by PGA. (a) Final image. (b) Range compressed image.
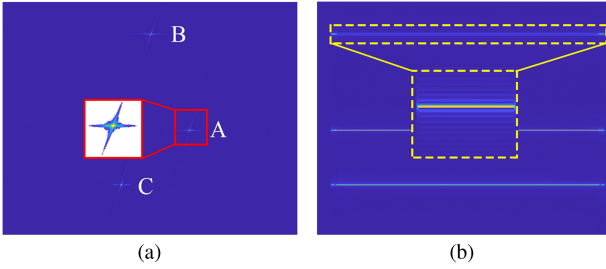

Fig. 16. Refocused results by the proposed 2-D autofocus method. (a) Final image. (b) Range compressed image.
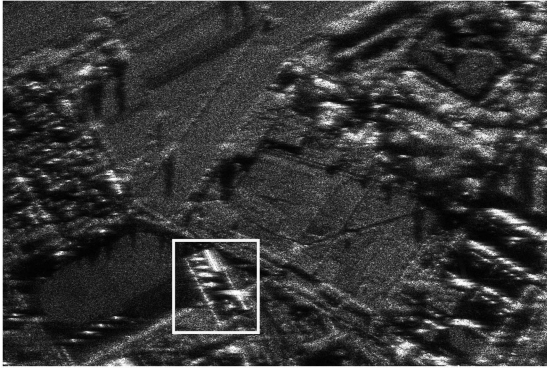

Fig. 17. Generated imagery with the PGA.

and 16(a). It is apparent that the 2-D defocus is well restrained by utilizing the presented 2-D autofocus scheme.

2) Real Data Experiments: To further verify the proposed 2-D autofocus method, the real data experiments are conducted in this section. The used data is obtained by a spotlight SAR sensor with a squint angle of about $35°$. The resolution of the formed image is about 0.35 m $\times$ 0.26 m (range $\times$ azimuth). Prior to autofocus processing, a serious deviated trajectory is adopted for TSST to preprocessing the raw data, then different autofocus techniques are applied to enhance the focusing quality.

First, classical 1-D PGA is adopted to improve the image quality and the corresponding processing result is depicted in Fig. 17. Cause of the phase error is spread across several range resolution cells and the PGA can only obtain and compensate
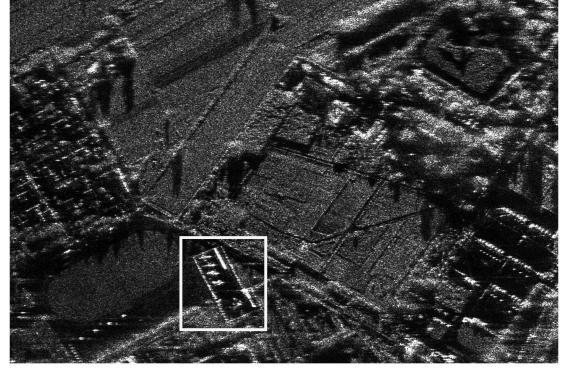

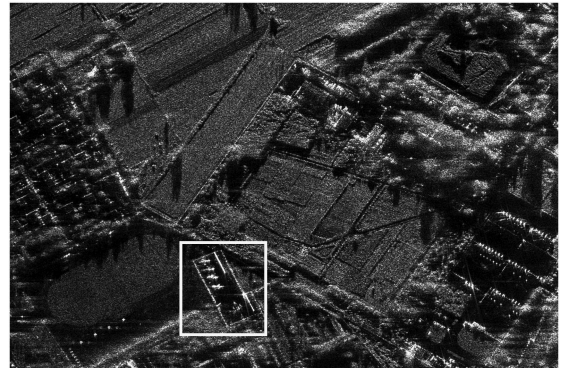Fig. 18. Generated imagery with the 2-D PGA-RRD.

Fig. 19. Generated imagery with the proposed algorithm.

for the 1-D APE, the remaining defocus effect is still can be easily observed in Fig. 17.

In order to alleviate the impact of the remaining RCM to the 1-D APE estimation, range resolution decreasing technique [14], [30] is adopted to improve the error estimation accuracy of the 1-D APE, which uses merely a small fraction of the collected data to estimate the APE. Then, 2-D autofocus is utilized to improve the quality of the defocused imagery by mapping the estimated APE into the 2-D phase error with (25). After this autofocus processing (named 2-D PGA-RRD), the generated SAR image is exhibited in Fig. 18. Compared to the result of the 1-D autofocus in Fig. 16, it can be seen that the focusing quality has been improved. To further improve the image quality, the presented 2-D autofocus scheme is applied and the corresponding processing result is shown in Fig. 19. To give a detailed comparison, the magnified areas marked in Figs. 17–19 are exhibited in Fig. 20. Therefore, the experiments indicate that the proposed algorithm is effective and superior to the compared algorithms.

VI. DISCUSSIONS

In the above sections, the TSST and the corresponding 2-D phase error structure are analyzed and verified. Because of the planar wavefront approximation, the image quality of TSST will be inevitably affected by the defocus and distortion problems. In
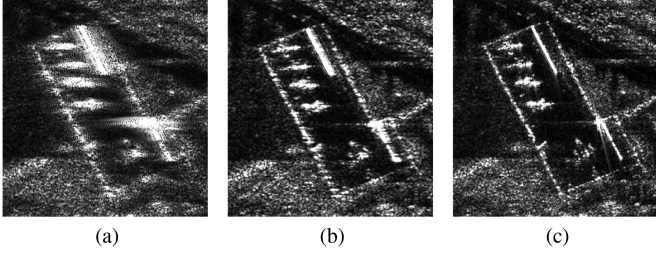
Fig. 20. Enlarged areas marked in Figs. 17–19. (a) Enlarged areas marked in Fig. 17. (b) Enlarged areas marked in Fig. 18. (c) Enlarged areas marked in Fig. 19.

this section, the correction for the defocus and distortion induced by the planar wavefront assumption are discussed.

To mitigate the effects caused by the planar wavefront approximation, the space-variant post-filtering algorithm (SVPF) [31], [32], [33] is regarded as the typical approach to compensate for the image deterioration. Different filter functions are proposed aiming at different imaging conditions. Another method [34], [35], [36] is to divide the illuminated area into multiple subregions and apply different phase corrections to the phase history data before resampling processing. There are more literatures are readily available about corrections to the planar wavefront approximation error. We do not want to despise the unmentioned literatures here, but just show that there are too many to list.

Because of the defocus effect is mainly caused by the quadratic term of the wavefront curvature error, we merely focus on corrections for the quadratic phase error under the framework of SVPF in this section.

Without planar wavefront assumption, the second-order Taylor series expansion to the differential range $\Delta R = R_a - R_t$ with respect to slow time t can be expressed as

$$\Delta R \approx \Delta R^{(0)} + \Delta R^{(1)} \cdot t + \Delta R^{(2)} \cdot \frac{1}{2} t^2 \qquad (29)$$

where $\Delta R^{(n)}$ represents the coefficient of the nth-order Taylor series terms of ΔR.

Under the planar wavefront assumption, the point actually located at (x_p, y_p) will appear at $(\hat{x}, \hat{y})$ in the formed image. Therefore, take the distorted location into consideration, the differential range of (3) can also be defined as

$$\Delta R_p = \cos\varphi \sin\theta \cdot \hat{x} + \cos\varphi \cos\theta \cdot \hat{y}$$
$$= \frac{x_a}{R_a} \cdot \hat{x} + \frac{y_a}{R_a} \cdot \hat{y}. \qquad (30)$$

Similarly, the second-order Taylor series expansion to the differential range ΔR_p can be expressed as

$$\Delta R_p \approx \Delta R_p^{(0)} + \Delta R_p^{(1)} \cdot t + \Delta R_p^{(2)} \cdot \frac{1}{2} t^2 \qquad (31)$$

where $\Delta R_p^{(n)}$ represents the coefficient of the nth-order Taylor series terms of ΔR_p.

It should note that the location of the point target in the formed image is determined by the constant and linear terms, $\Delta R^{(0)}$ and $\Delta R^{(1)}$ of ΔR, $\Delta R_p^{(0)}$ and $\Delta R_p^{(1)}$ of ΔR_p. According to [37], when the geometric distortion is considered in the approximate

TABLE IV
SIMULATION PARAMETERS

Parameters	Values	Parameters	Values
Pulse duration	2 μs	Wavelength	0.03 m
PRF	1200 Hz	Range band width	750 MHz
Squint angle θ_s	30°	Working distance	5 km
Height	1 km	Radar velocity	60 m/s

differential range in (30), we have

$$\begin{cases} \Delta R^{(0)} = \Delta R_p^{(0)} \\ \Delta R^{(1)} = \Delta R_p^{(1)} \end{cases}. \qquad (32)$$

Then, we have

$$\begin{cases} \hat{y} = \frac{A-B}{\cos\varphi_0} \\ \hat{x} = \frac{C-D-E\hat{y}}{F} \end{cases} \qquad (33)$$

where

$$A = \sqrt{R_g^2 + H^2}$$
$$B = \sqrt{x_p^2 + (R_g - y_p)^2 + H^2}$$
$$C = \frac{R_g v \sin\theta_s}{A}$$
$$D = \frac{-x_p v \cos\theta_s + (R_g - y_p)v \sin\theta_s}{B}$$
$$E = \frac{v \sin\theta_s A - R_g C}{A^2}$$
$$F = \frac{v \cos\theta_s}{A}$$

Equation (33) gives the mapping relations between the real and the distorted locations of the targets. Then, the geometric distortion correction can be accomplished by resampling the distorted point from the wrong position $(\hat{x}, \hat{y})$ to the right position (x_p, y_p) to generate an undistorted image.

According to [37], the residual quadratic phase error can be defined as

$$\Phi_q = \frac{4\pi}{\lambda}\left[\frac{1}{2}\Delta R^{(2)} - \frac{1}{2}\Delta R_p^{(2)}\right]\cdot t^2 \qquad (34)$$

where λ is the wavelength and

$$\Delta R^{(2)} = \frac{v^2 - C^2}{A} + \frac{D^2 - v^2}{B}$$
$$\Delta R_p^{(2)} = \hat{x}\frac{2v\cos\theta_s C}{A^2} + \hat{y}\frac{R_g A\frac{v^2 - C^2}{A} - 2R_g C^2 + 2ACv\sin\theta_s}{A^3}.$$

Then, the conjugation of (34) can be used as the filter function of the SVPF to enlarge the focused scope, the specific implementation steps can be seen in [31].

The simulated experiments are executed based on the above analysis. The adoptive parameters used in the simulation is shown in Table IV. The simulated azimuth resolution is $0.2\,m$. Take $\pi/2$ as the allowable quadratic phase error under the planar wavefront approximation [3], the effective imaging scene radius is only about $163\,m$ for the given parameters. The distribution of nine simulated targets is specified in Fig. 21. Except the target in the scene center, the residual eight targets are $400\,m$ away from
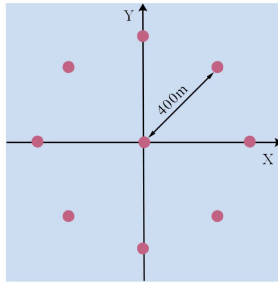
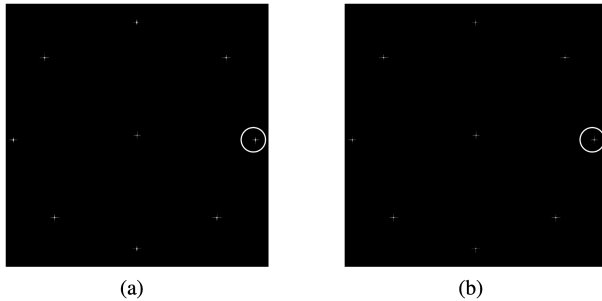Fig. 21. Distribution of the simulated targets.

Fig. 22. Imaging results. (a) Imaging result of TSST. (b) Imaging result after applying SVPF to (a).
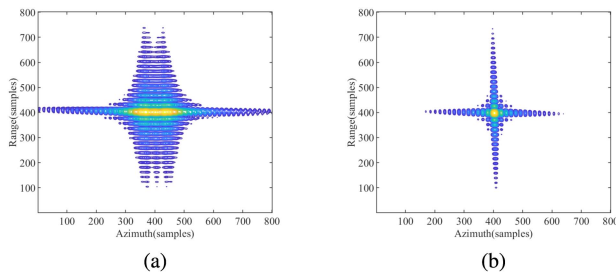

Fig. 23. Contour plots of the white circle marked points in Fig. 22. (a) Contour plots of the white circle marked point in Fig. 22(a). (b) Contour plots of the white circle marked point in Fig. 22(b).

the scene center, which is far greater than the allowable radius. Fig. 22 gives the imaging results with and without correcting the residual quadratic phase error. For a detailed comparison, the contour plots of the white circles marked points in Fig. 22(a) and (b) are exhibited in Fig. 23. It can be seen that the evident azimuth defocus is appeared in Fig. 23(a), and this degradation is well compensated by using the filter function-based SVPF (34).

VII. Conclusion

This article presents a new imaging algorithm by combining two-step scaling transform with 2-D autofocus technique for processing the squint spotlight SAR echo. The planar wavefront assumption forms the foundation of this algorithm, then a modified range-frequency linear scaling transform and an azimuth-time nonlinear scaling transform are presented to eliminate the coupling between the range-frequency and azimuth-time.

Meanwhile, to improve the efficiency and avoid spectrum aliasing, a scaling factor aided MRFLST is implemented by the PCS, which involves only complex multiplications and FFTs without any interpolation. Next, to remove the 2-D defocus effects caused by the deviation of range measurement and atmospheric propagation effects, 2-D phase error structure implied in the proposed TSST is explored. Finally, the correction for the defocus and distortion induced by the planar wavefront assumption are analyzed and verified. The performance of the proposed algorithm is demonstrated by the simulated and real experiments.

References

[1] D. A. Ausherman, A. Kozma, J. L. Walker, H. M. Jones, and E. C. Poggio, "Developments in radar imaging," *IEEE Trans. Aerosp. Electron. Syst.*, vol. AES- 20, no. 4, pp. 363–400, Jul. 1984.

[2] P. A. Thompson, D. E. Wahl, P. H. Eichel, D. C. Ghiglia, and C. V. Jakowatz, *Spotlight-Mode Synthetic Aperture Radar: A Signal Processing Approach*. Berlin, Germany: Springer, 1996.

[3] W. G. Carrara, R. S. Goodman, and R. M. Majewski, *Spotlight Synthetic Aperture Radar: Signal Processing Algorithms*. Norwood, MA, USA: Artech House 1995.

[4] M. Denny and I. Scott, "Anomalous propagation limitations to high-resolution SAR performance," in *Proc. IEEE Radar Conf.*, 2002, pp. 249–254.

[5] X. Mao, D. Zhu, and Z. Zhu, "Autofocus correction of ape and residual RCM in spotlight SAR polar format imagery," *IEEE Trans. Aerosp. Electron. Syst.*, vol. 49, no. 4, pp. 2693–2706, Oct. 2013.

[6] D. W. Warner, D. C. Ghiglia, A. Fitzgerrell, and J. Beaver, "Two-dimensional phase gradient autofocus," in *Image Reconstruction From Incomplete Data*, M. A. Fiddy and R. P. Millane, Eds., vol. 4123. Bellingham, WA, USA: SPIE, 2000, pp. 162–173, doi: 10.1117/12.409267.

[7] A. W. Doerry, "Autofocus correction of excessive migration in synthetic aperture radar images," 2004. [Online]. Available: https://www.osti.gov/biblio/919639

[8] J.-T. González-Partida, P. Almorox-González, M. Burgos-Garcia, and B.-P. Dorta-Naranjo, "SAR system for UAV operation with motion error compensation beyond the resolution cell," *Sensors*, vol. 8, no. 5, pp. 3384–3405, 2008. [Online]. Available: https://www.mdpi.com/1424-8220/8/5/3384

[9] N. Li, R. Wang, Y. Deng, W. Yu, Z. Zhang, and Y. Liu, "Autofocus correction of residual RCM for VHR SAR sensors with light-small aircraft," *IEEE Trans. Geosci. Remote Sens.*, vol. 55, no. 1, pp. 441–452, Jan. 2017.

[10] J. Chen, B. Liang, D.-G. Yang, D.-J. Zhao, M. Xing, and G.-C. Sun, "Two-step accuracy improvement of motion compensation for airborne SAR with ultrahigh resolution and wide swath," *IEEE Trans. Geosci. Remote Sens.*, vol. 57, no. 9, pp. 7148–7160, Sep. 2019.

[11] X. Mao, X. He, and D. Li, "Knowledge-aided 2-D autofocus for spotlight SAR range migration algorithm imagery," *IEEE Trans. Geosci. Remote Sens.*, vol. 56, no. 9, pp. 5458–5470, Sep. 2018.

[12] H. Lin, J. Chen, M. Xing, X. Chen, D. You, and G. Sun, "2-D frequency autofocus for squint spotlight SAR imaging with extended omega-K," *IEEE Trans. Geosci. Remote Sens.*, vol. 60, Jul. 2021, Art. no. 5211312.

[13] X. Mao, L. Ding, Y. Zhang, R. Zhan, and S. Li, "Knowledge-aided 2-D autofocus for spotlight SAR filtered backprojection imagery," *IEEE Trans. Geosci. Remote Sens.*, vol. 57, no. 11, pp. 9041–9058, Nov. 2019.

[14] X. Mao and D. Zhu, "Two-dimensional autofocus for spotlight SAR polar format imagery," *IEEE Trans. Comput. Imag.*, vol. 2, no. 4, pp. 524–539, Dec. 2016.

[15] P. A. Makarov, "Two-dimensional autofocus technique based on spatial frequency domain fragmentation," *IEEE Trans. Image Process.*, vol. 29, pp. 6006–6016, Apr. 2020.

[16] I. Cumming and F. Wong, *Digital Processing of Synthetic Aperture Radar Data: Algorithms and Implementation*. Norwood, MA, USA: Artech House, 2005.

[17] R. K. Raney, H. Runge, R. Bamler, I. G. Cumming, and F. H. Wong, "Precision SAR processing using chirp scaling," *IEEE Trans. Geosci. Remote Sens.*, vol. 32, no. 4, pp. 786–799, Jul. 1994.

[18] M. Xing, Y. Wu, Y. D. Zhang, G.-C. Sun, and Z. Bao, "Azimuth re-sampling processing for highly squinted synthetic aperture radar imaging with several modes," *IEEE Trans. Geosci. Remote Sens.*, vol. 52, no. 7, pp. 4339–4352, Jul. 2014.

[19] L. M. H. Ulander, H. Hellsten, and G. Stenstrom, "Synthetic-aperture radar processing using fast factorized back-projection," *IEEE Trans. Aerosp. Electron. Syst.*, vol. 39, no. 3, pp. 760–776, Jul. 2003.

[20] S. Zhou, L. Yang, L. Zhao, and G. Bi, "Quasi-polar-based FFBP algorithm for miniature UAV SAR imaging without navigational data," *IEEE Trans. Geosci. Remote Sens.*, vol. 55, no. 12, pp. 7053–7065, Dec. 2017.

[21] Q. Dong, G. Sun, Z. Yang, L. Guo, and M. Xing, "Cartesian factorized backprojection algorithm for high-resolution spotlight SAR imaging," *IEEE Sensors J.*, vol. 18, no. 3, pp. 1160–1168, Feb. 2018.

[22] Y. Luo, F. Zhao, N. Li, and H. Zhang, "A modified cartesian factor-ized back-projection algorithm for highly squint spotlight synthetic aper-ture radar imaging," *IEEE Geosci. Remote Sens. Lett.*, vol. 16, no. 6, pp. 902–906, Jun. 2019.

[23] S. Tang, H. Deng, P. Guo, Y. Li, and L. Zhang, "Generalized PFA for air-missile borne bistatic forward-looking beam-steering SAR with accelerations," *IEEE Access*, vol. 6, pp. 74616–74627, 2018.

[24] F. Wang, L. Zhang, Y. Cao, T.-S. Yeo, and G. Wang, "A novel algorithm for hypersonic SAR imaging with large squint angle and dive trajectory," *IEEE Geosci. Remote Sens. Lett.*, vol. 19, Aug. 2021, Art. no. 4016105.

[25] A. Gao, B. Sun, J. Li, and C. Li, "A parameter-adjusting autoregistration imaging algorithm for video synthetic aperture radar," *IEEE Trans. Geosci. Remote Sens.*, vol. 60, Oct. 2021, Art. no. 5215414.

[26] S. Han, D. Zhu, and X. Mao, "Residual high-order wavefront curvature error compensation for the polar format algorithm in widefield spotlight SAR imaging," *Remote Sens. Lett.*, vol. 12, no. 9, pp. 910–920, Aug. 2021.

[27] D. Zhu, S. Ye, and Z. Zhu, "Polar format algorithm using chirp scaling for spotlight SAR image formation," *IEEE Trans. Aerosp. Electron. Syst.*, vol. 44, no. 4, pp. 1433–1448, Oct. 2008.

[28] X. Nie, D. Zhu, X. Mao, and Z. Zhu, "The application of the principle of chirp scaling in processing stepped chirps in spotlight SAR," *IEEE Geosci. Remote Sens. Lett.*, vol. 6, no. 4, pp. 860–864, Oct. 2009.

[29] Y. Miao, J. Wu, and J. Yang, "Azimuth migration-corrected phase gradient autofocus for bistatic SAR polar format imaging," *IEEE Geosci. Remote Sens. Lett.*, vol. 18, no. 4, pp. 697–701, Apr. 2021.

[30] A. W. Doerry, F. E. Heard, and J. T. Cordaro, "Decreasing range resolution of a SAR image to permit correction of motion measurement errors beyond the SAR range resolution," U.S. Patent 7760128, Jul. 20, 2010.

[31] A. W. Doerry, "Wavefront curvature limitations and compensation to polar format processing for synthetic aperture radar images," 2006. [Online]. Available: https://www.osti.gov/biblio/902879

[32] X. Mao, D. Zhu, and Z. Zhu, "Polar format algorithm wavefront curvature compensation under arbitrary radar flight path," *IEEE Geosci. Remote Sens. Lett.*, vol. 9, no. 3, pp. 526–530, May 2012.

[33] Y. Miao, J. Yang, J. Wu, Z. Sun, and T. Chen, "Spatially variable phase fil-tering algorithm based on azimuth wavenumber regularization for bistatic spotlight SAR imaging under complicated motion," *IEEE Trans. Geosci. Remote Sens.*, vol. 60, Dec. 2021, Art. no. 5223115.

[34] H.-S. Shin, J.-H. Jeon, and J.-T. Lim, "Airborne squinted spotlight SAR imaging using polar format algorithm," in *Proc. SICE-ICASE Int. Joint Conf.*, 2006, pp. 4182–4185.

[35] S. Paker, M. Kartal, and S. Kent, "A new subpatch focusing algorithm for spotlight SAR processing of large scenes," in *Proc. 8th Eur. Conf. Synthetic Aperture Radar*, 2010, pp. 1–4.

[36] R. Hu et al., "Refocusing and zoom-in polar format algorithm for curvi-linear spotlight SAR imaging on arbitrary region of interest," *IEEE Trans. Geosci. Remote Sens.*, vol. 57, no. 10, pp. 7995–8010, Oct. 2019.

[37] L. A. Gorham and B. D. Rigling, "Scene size limits for polar format algorithm," *IEEE Trans. Aerosp. Electron. Syst.*, vol. 52, no. 1, pp. 73–84, Feb. 2016.

Shengliang Han received the B.S. degree in elec-trical engineering and automation from the Qingdao University of Technology, Qingdao, China, in 2016 and the M.S. degree in electronic science and technol-ogy from Shandong Normal University, Jinan, China, in 2019. Since 2019, he has been working toward the Ph.D. degree in communication and information systems with the Key Laboratory of Radar Imaging and Microwave Photonics, Ministry of Education, Nanjing University of Aeronautics and Astronautics, Nanjing, China.

His research interests include signal processing and its applications in syn-thetic aperture radar (SAR) imaging.

Daiyin Zhu (Member, IEEE) received the B.S. degree from Southeast University, Nanjing, China, in 1996, and the M.S. and Ph.D. degrees from the Nanjing University of Aeronautics and Astronautics (NUAA), Nanjing, China, in 1998 and 2002, respectively, all in electronic engineering.

From 1998 to 1999, he was a Guest Scientist with the Institute of Radio Frequency Technology, German Aerospace Center, Weßling, Germany, where he worked in the field of synthetic aperture radar (SAR) interferometry. In 1998, he joined the De-partment of Electronic Engineering, NUAA, where he is a Professor. He has developed algorithms for several operational airborne SAR systems. His research interests include radar imaging algorithms, SAR/ISAR autofocus techniques, SAR ground moving target indication (SAR/GMTI), and SAR interferometry.

Xinhua Mao (Member, IEEE) received the B.S. and Ph.D. degrees in electronic engineering from the Nanjing University of Aeronautics and Astronautics (NUAA), Nanjing, China, in 2003 and 2009, respec-tively.

In 2009, he joined the Department of Electronic Engineering, NUAA, where he is a Full Professor with the Key Laboratory of Radar Imaging and Mi-crowave Photonics. He was a Visiting Scholar with Villanova University, Villanova, PA, USA, in 2013, and the University of Leicester, Leicester, U.K., from 2018 to 2019. He has developed algorithms for several operational airborne synthetic aperture radar (SAR) systems. His research interests include radar imaging, ground moving target indication (GMTI), and inverse problems.